Science Advances
AAAS

advances.sciencemag.org/cgi/content/full/4/7/eaat0788/DC1

Supplementary Materials for

Transition metal–assisted carbonization of small organic molecules toward functional carbon materials

Zhen-Yu Wu, Shi-Long Xu, Qiang-Qiang Yan, Zhi-Qin Chen, Yan-Wei Ding, Chao Li, Hai-Wei Liang*, Shu-Hong Yu*

*Corresponding author. Email: hwliang@ustc.edu.cn (H.-W.L.); shyu@ustc.edu.cn (S.-H.Y.)

Published 27 July 2018, *Sci. Adv.* **4**, eaat0788 (2018)
DOI: 10.1126/sciadv.aat0788

This PDF file includes:

Fig. S22. HER polarization curves of CM-*o*PD/Co/SiO_2 and CM-*o*PD/CoCu/SiO_2 in 0.5 M H_2SO_4.
Table S1. Summary of carbon yield, texture properties, elemental composition of CMs prepared with $Co(NO_3)_2$ as the catalyst.
Table S2. Carbon yields of *o*PD with different TMSs as catalysts.
Table S3. Carbon yields of *o*PD with different amounts of $Co(NO_3)_2$ as catalysts.
Table S4. Summary of carbon yield, texture properties, and elemental composition of CMs prepared with $Co(NO_3)_2$ as the catalyst and SiO_2 nanoparticles as hard templates.
Table S5. HER performance comparison.
Note S1. The proposed mechanism for different microstructures of CM-*x*/Co samples.
Note S2. Synthesis of high–surface area CMs from SOMs with SBA-15 as templates.
Note S3. Detailed characterization analysis of CM-Phen/Co, CM-Phen/Co/SiO_2, CM-DBrPhen/Co, and CM-DBrPhen/Co/SiO_2.
Note S4. Electrocatalytic performance of CMs for ORR.
References (*55*–*65*)

Supplementary Materials:

Fig. S1 to S22, Table S1 to S5 and Notes S1 to S4

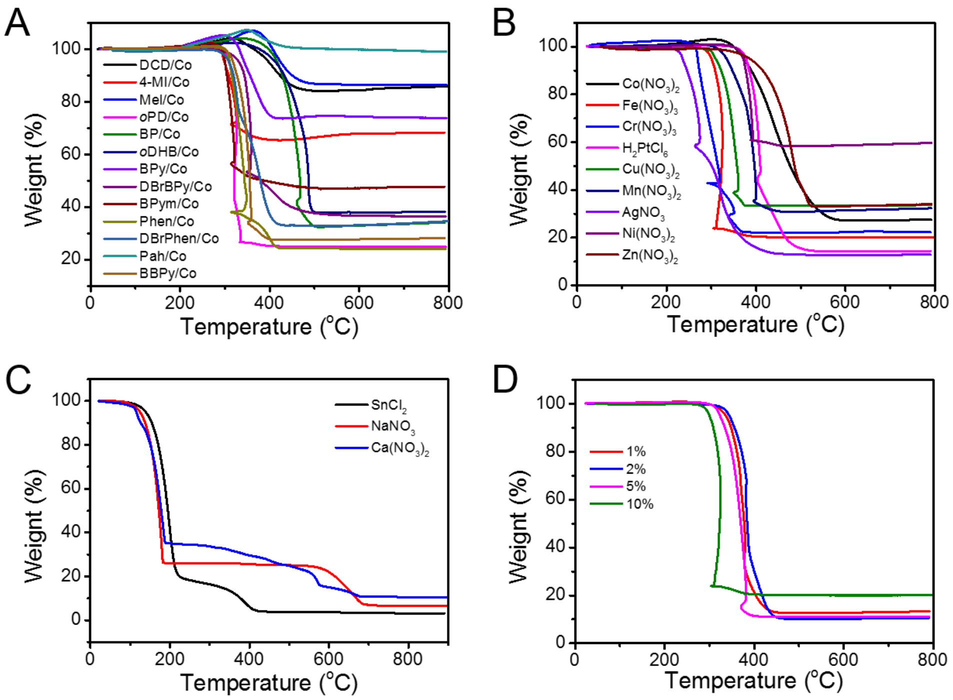

Fig. S1. TGA analyses. (A) TGA curves of different SOMs with $Co(NO_3)_2$ in O_2 atmosphere after TGA tests in N_2. **(B)** TGA curves of *o*PD with different TMSs in O_2 atmosphere after TGA tests in N_2. **(C)** TGA curves of *o*PD with three non-TMSs in N_2 atmosphere. **(D)** TGA curves of *o*PD with different $Co(NO_3)_2$ contents in O_2 atmosphere after TGA tests in N_2.

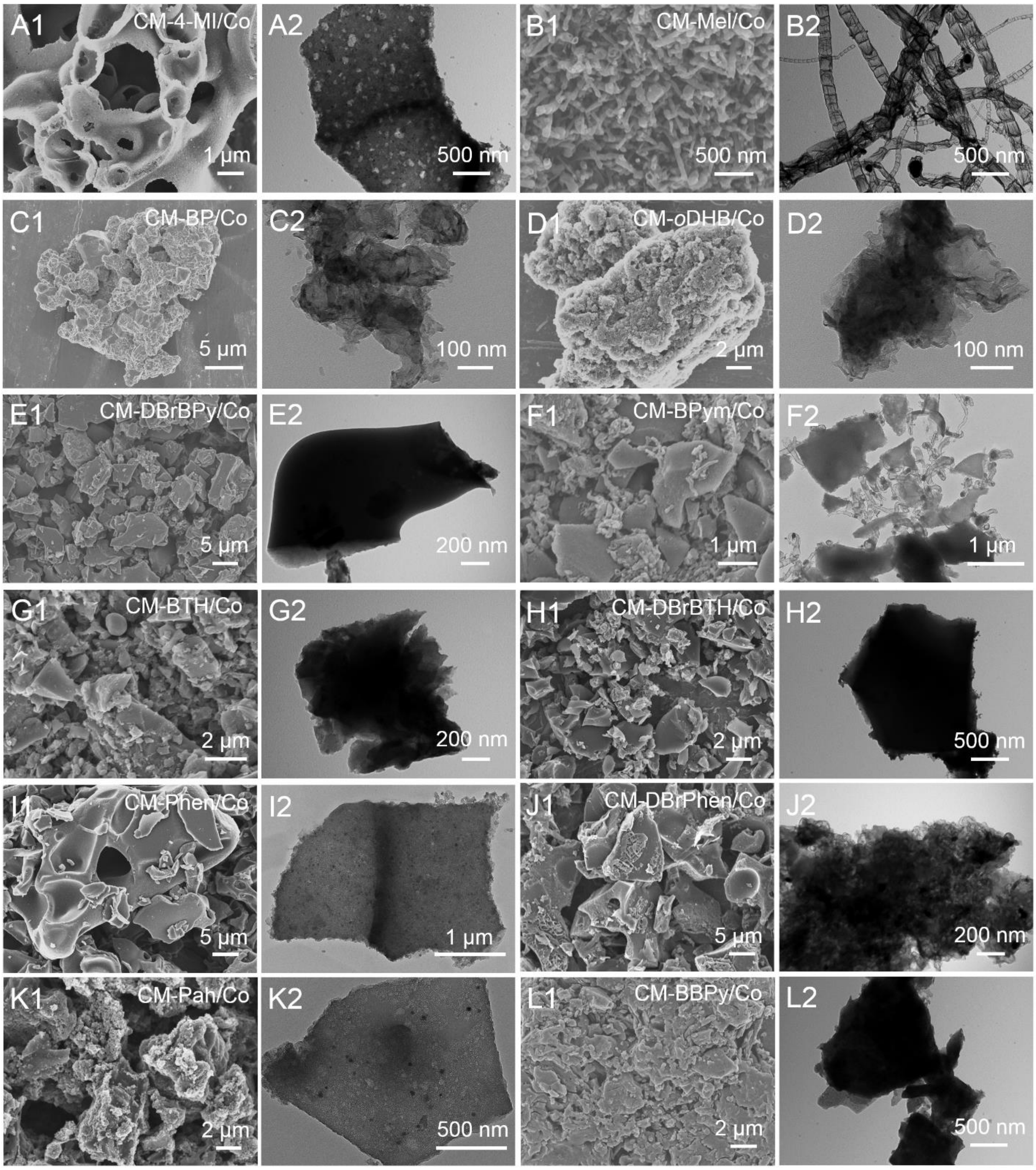

Fig. S2. SEM and TEM images of CM-*x*/Co samples. (A to **L)** CM-4-MI/Co, CM-Mel/Co, CM-BP/Co, CM-*o*DHB/Co, CM-DBrBPy/Co, CM-BPym/Co, CM-BTh/Co, CM-DBrBTh/Co, CM-Phen/Co, CM-DBrPhen/Co, CM-Pah/Co, and CM-BBPy/Co.

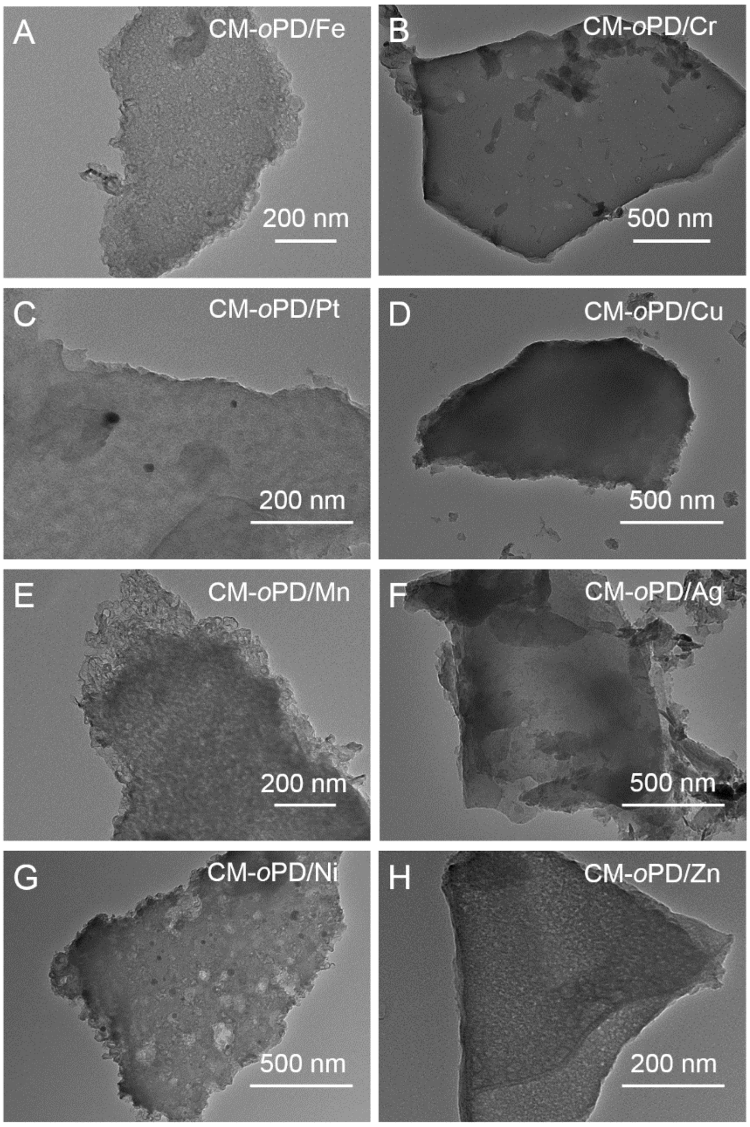

Fig. S3. TEM images of *o*PD-derived CMs prepared with different TMSs. (A to **H)** TEM images of *o*PD-derived CMs prepared with different TMSs: $Fe(NO_3)_3$, $Cr(NO_3)_3$, H_2PtCl_6, $Cu(NO_3)_2$, $Mn(NO_3)_2$, $AgNO_3$, $Ni(NO_3)_2$, and $Zn(NO_3)_2$.

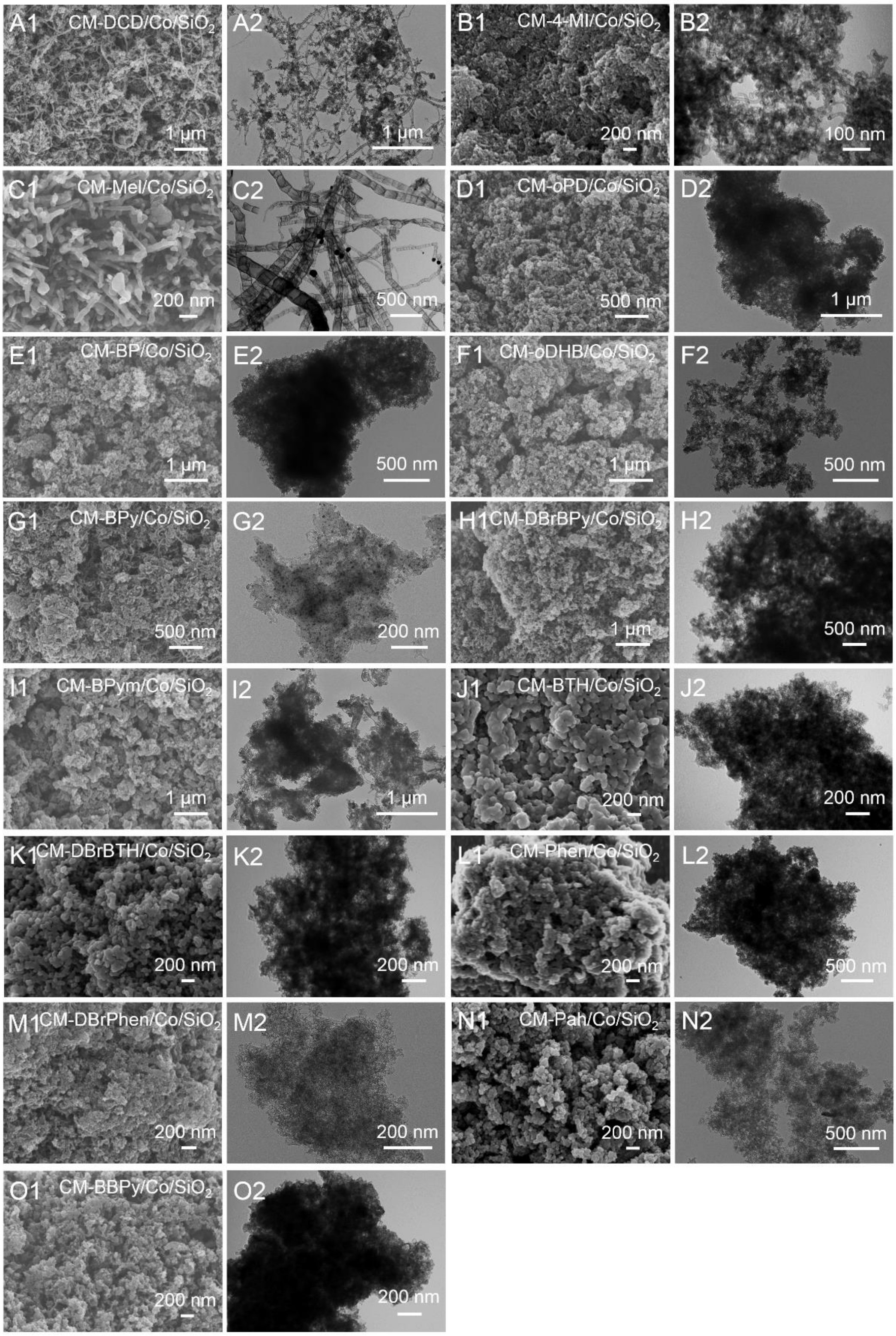

Fig. S4. SEM and TEM images of SiO$_2$-templating CMs. (A to **O)** CM-DCD/Co/SiO$_2$, CM-4-MI/Co/SiO$_2$, CM-Mel/Co/SiO$_2$, CM-*o*PD/Co/SiO$_2$, CM-BP/Co/SiO$_2$, CM-*o*DHB/Co/SiO$_2$, CM-BPy/Co/SiO$_2$, CM-DBrBPy/Co/SiO$_2$, CM-BPym/Co/SiO$_2$, CM-BTh/Co/SiO$_2$, CM-DBrBTh/Co/SiO$_2$, CM-Phen/Co/SiO$_2$, CM-DBrPhen/Co/SiO$_2$, CM-Pah/Co/SiO$_2$, and CM-BBPy/Co/SiO$_2$.

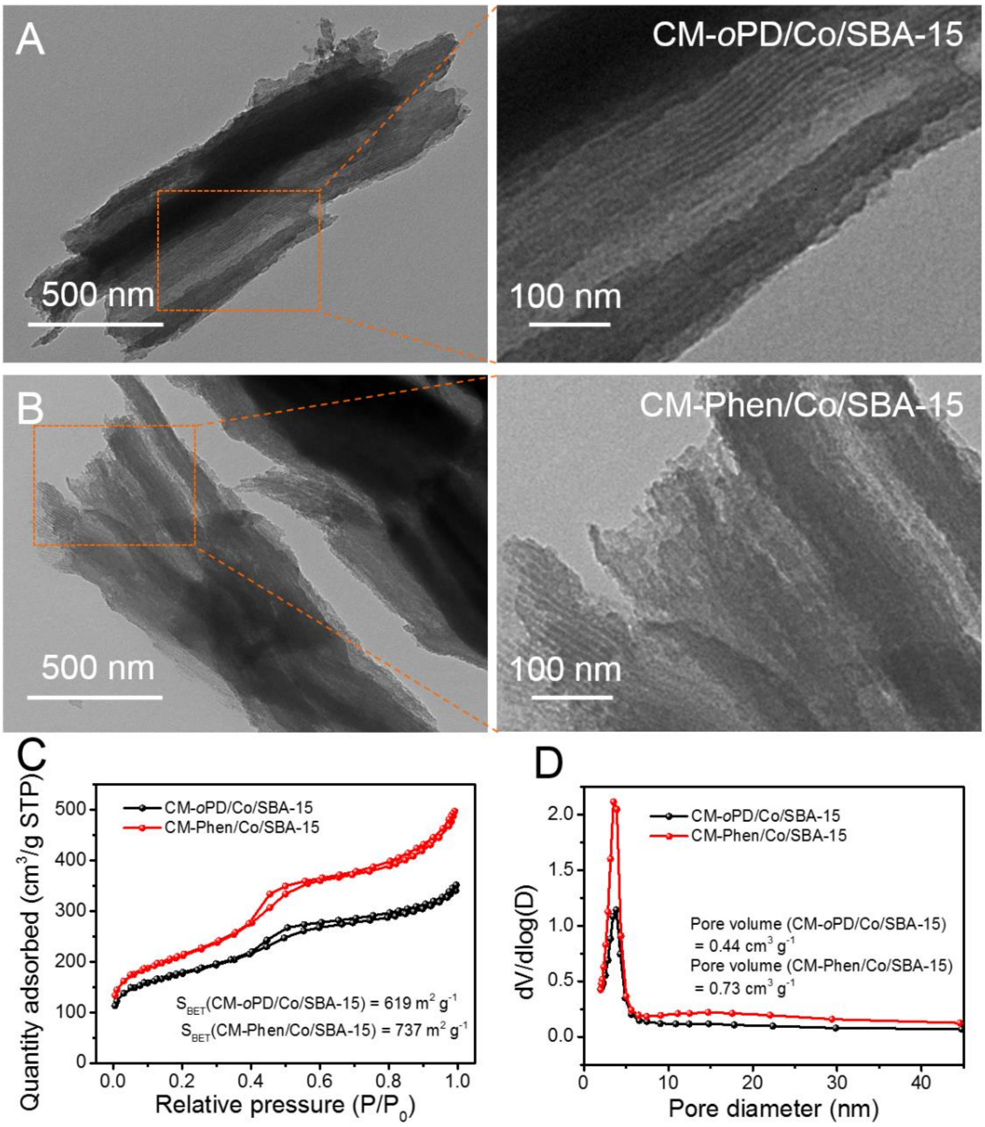

Fig. S5. Characterizations of CM-*o*PD/Co/SBA-15, and CM-Phen/Co/SBA-15. (A and **B)** TEM images of **(A)** CM-*o*PD/Co/SBA-15, and **(B)** CM-Phen/Co/SBA-15. **(C)** Nitrogen adsorption/desorption isotherms, and **(D)** PSD curves of CM-*o*PD/Co/SBA-15 and CM-Phen/Co/SBA-15.

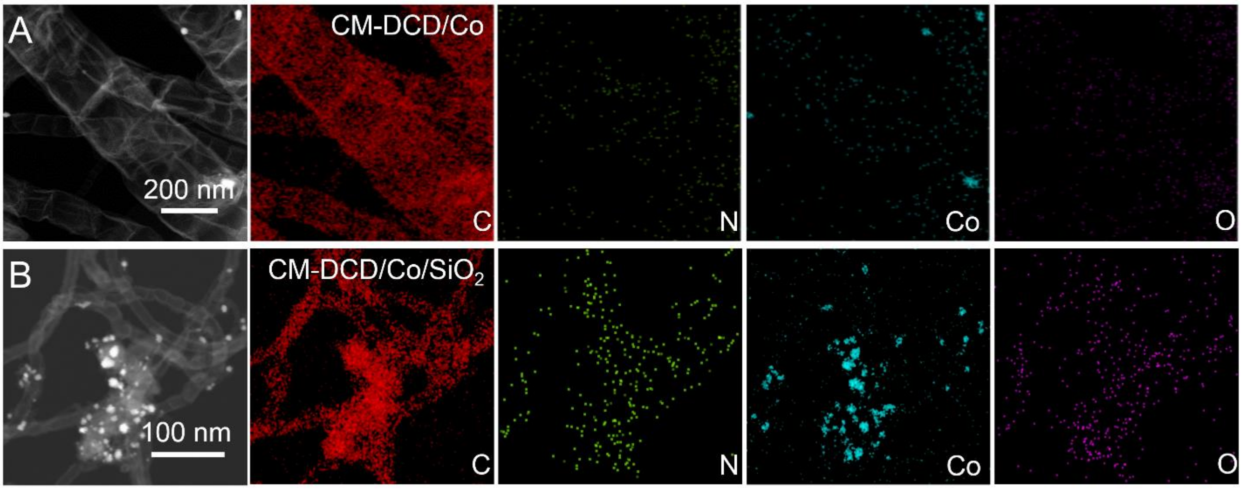

Fig. S6. STEM-EDS elemental mapping images of CM-DCD/Co and CM-DCD/Co/SiO$_2$. (A and **B)** STEM-EDS elemental mapping images of (**A**) CM-DCD/Co and (**B**) CM-DCD/Co/SiO$_2$.

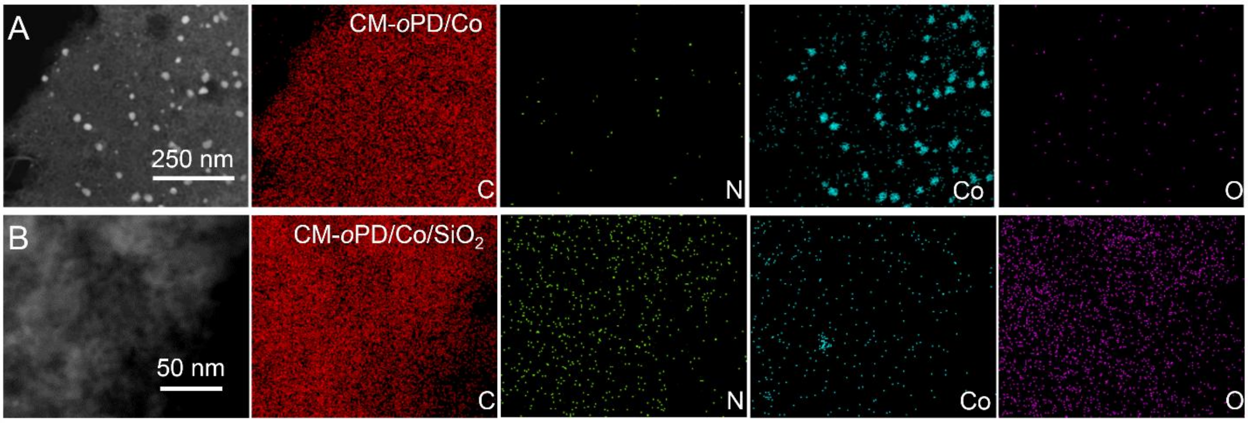

Fig. S7. STEM-EDS elemental mapping images of CM-*o*PD/Co and CM-*o*PD/Co/SiO$_2$. (A and B) STEM-EDS elemental mapping images of **(A)** CM-*o*PD/Co and **(B)** CM-*o*PD/Co/SiO$_2$.

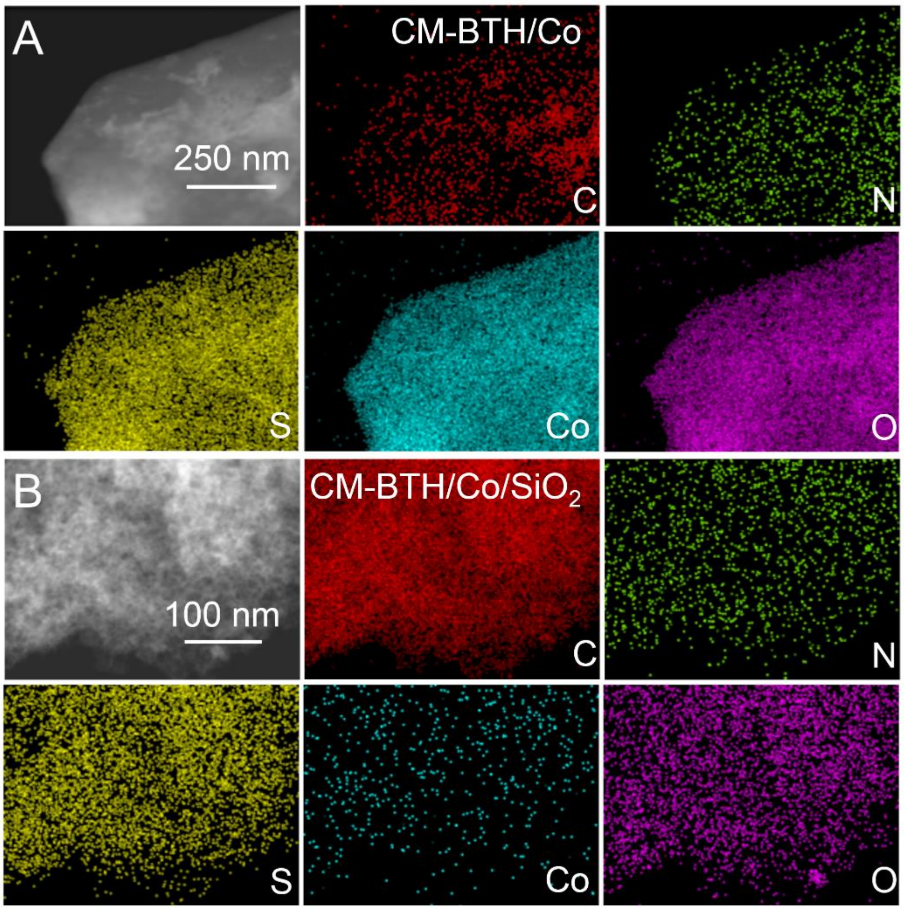

Fig. S8. STEM-EDS elemental mapping images of CM-BTH/Co and CM-BTH/Co/SiO$_2$. (A and B) STEM-EDS elemental mapping images of **(A)** CM-BTH/Co and **(B)** CM-BTH/Co/SiO$_2$.

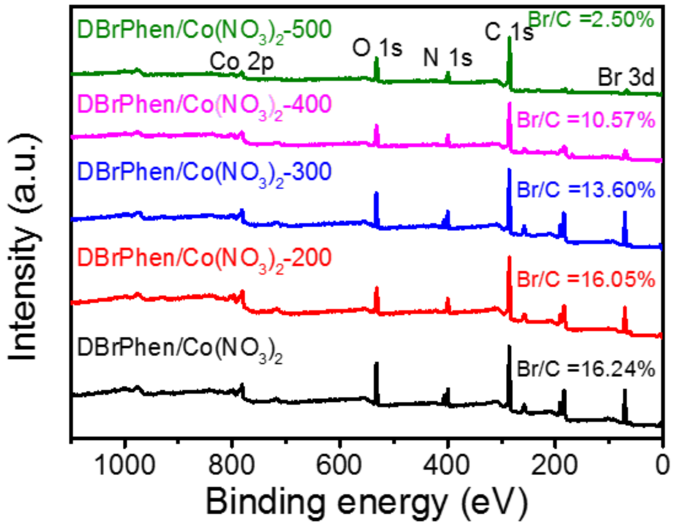

Fig. S9. XPS survey spectra of the DBrPhen/Co(NO_3)$_2$ precursor and its carbonization products obtained at 200° to 500°C.

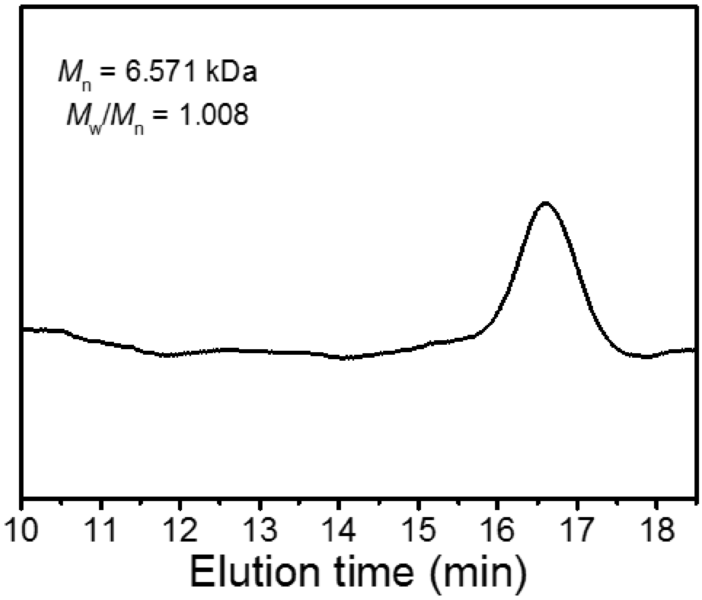

Fig. S10. GPC result of the sample that prepared by heating DBrPhen with Co(NO_3)$_2$ at 250°C for 0.5 hours under N_2. This data revealed that the carbonization product at low temperature consisted of high molecular weight polymeric species with a number-average molecular weight (M_n) of 6.571 kDa and a relatively narrow size range (low polydispersity, polydispersity = M_w/M_n, where M_w represents weight average molecular weight).

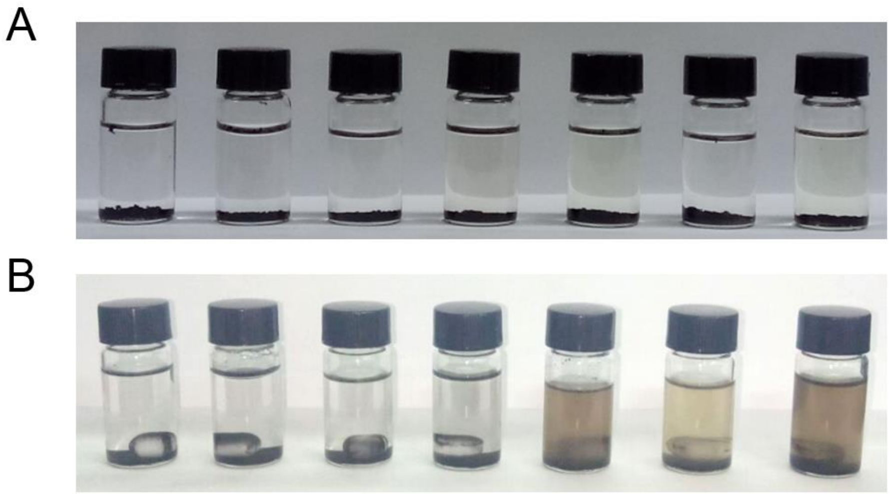

Fig. S11. Images of dispersing carbonization product obtained by heating DBrPhen with $Co(NO_3)_2$ at 400°C for 2 hours under N_2. (A) before stirring; **(B)** after stirring for one day. Solvents (from left to right): alcohol, water, acetone, dimethyl formamide, trichloromethane, tetrahydrofuran and dimethylsulfoxide.

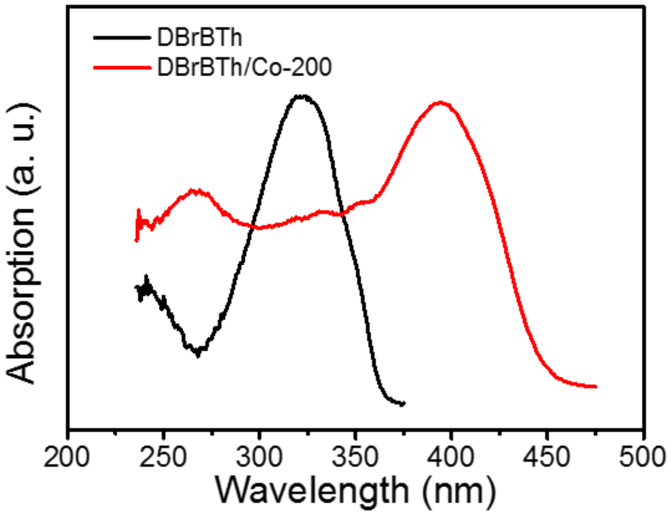

Fig. S12. UV-vis absorption spectra for DBrBTh and the carbonization product obtained by heating BTh/$Co(NO_3)_2$ at 200°C for 0.5 hours under N_2.

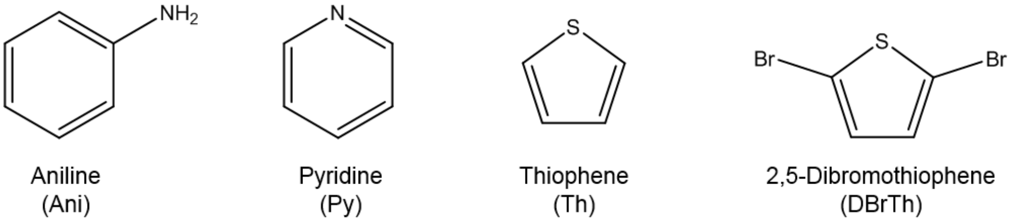

Fig. S13. The structures of four SOMs that could not be converted into CMs.

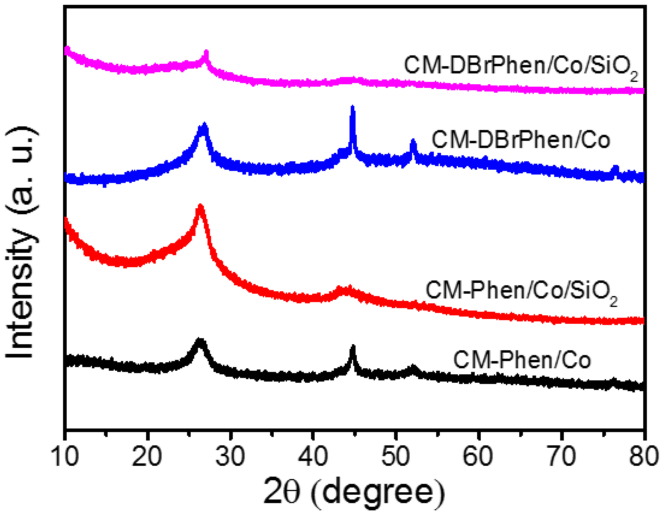

Fig. S14. XRD patterns of CM-Phen/Co, CM-Phen/Co/SiO_2, CM-DBrPhen/Co, and CM-DBrPhen/Co/SiO_2.

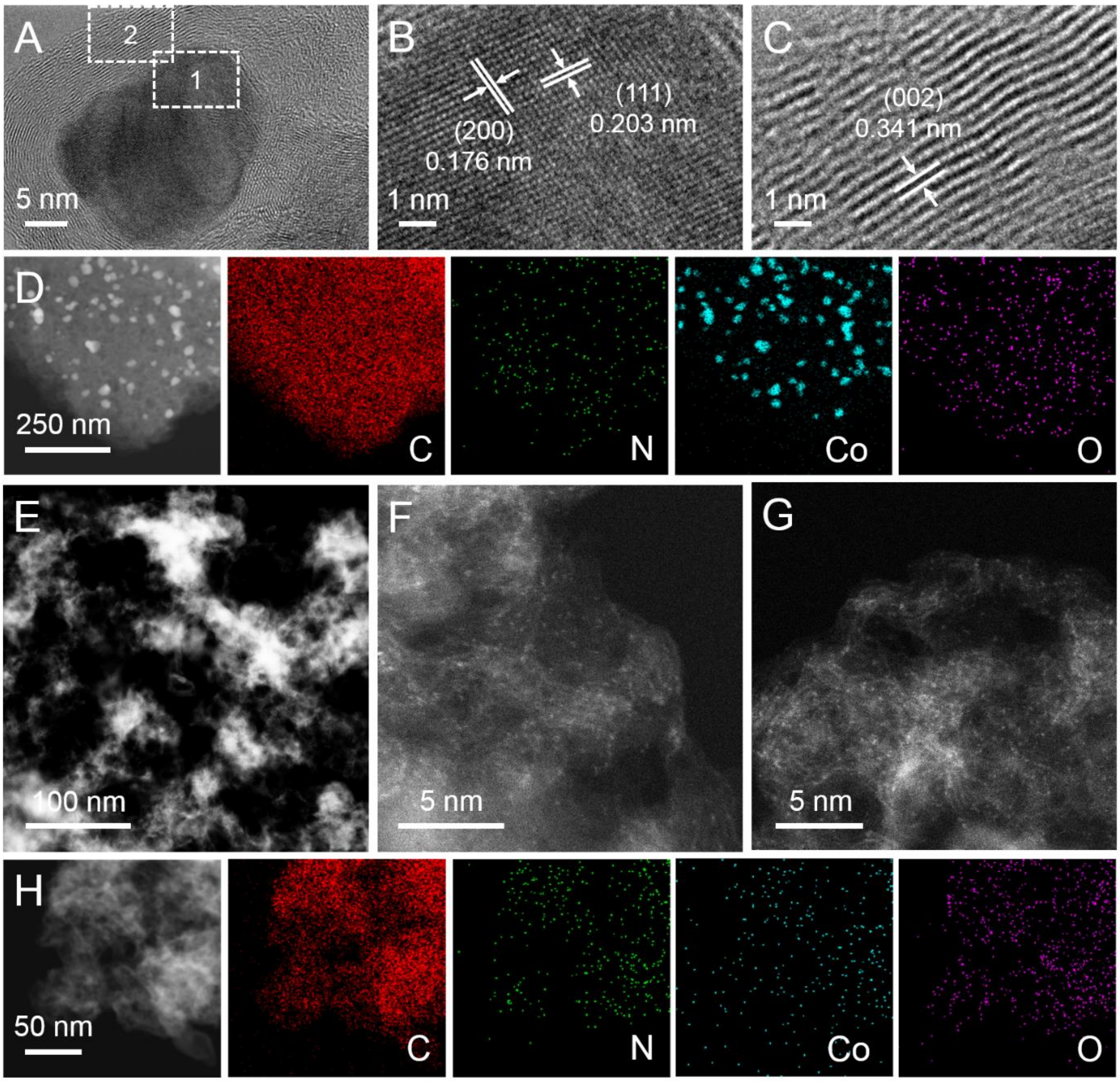

Fig. S15. Detailed characterizations of CM-Phen/Co and CM-Phen/Co/SiO$_2$ catalysts. (A) HRTEM image of CM-Phen/Co; **(B)** Magnified HRTEM image of section 1 in **A**; **(C)** Magnified HRTEM image of section 2 in **A**; **(D)** STEM-EDS elemental mapping images of CM-Phen/Co; **(E)** HAADF-STEM image of CM-Phen/Co/SiO$_2$; **(F, G)** aberration-corrected HAADF-STEM images of CM-Phen/Co/SiO$_2$; **(H)** STEM-EDS elemental mapping images of CM-Phen/Co/SiO$_2$.

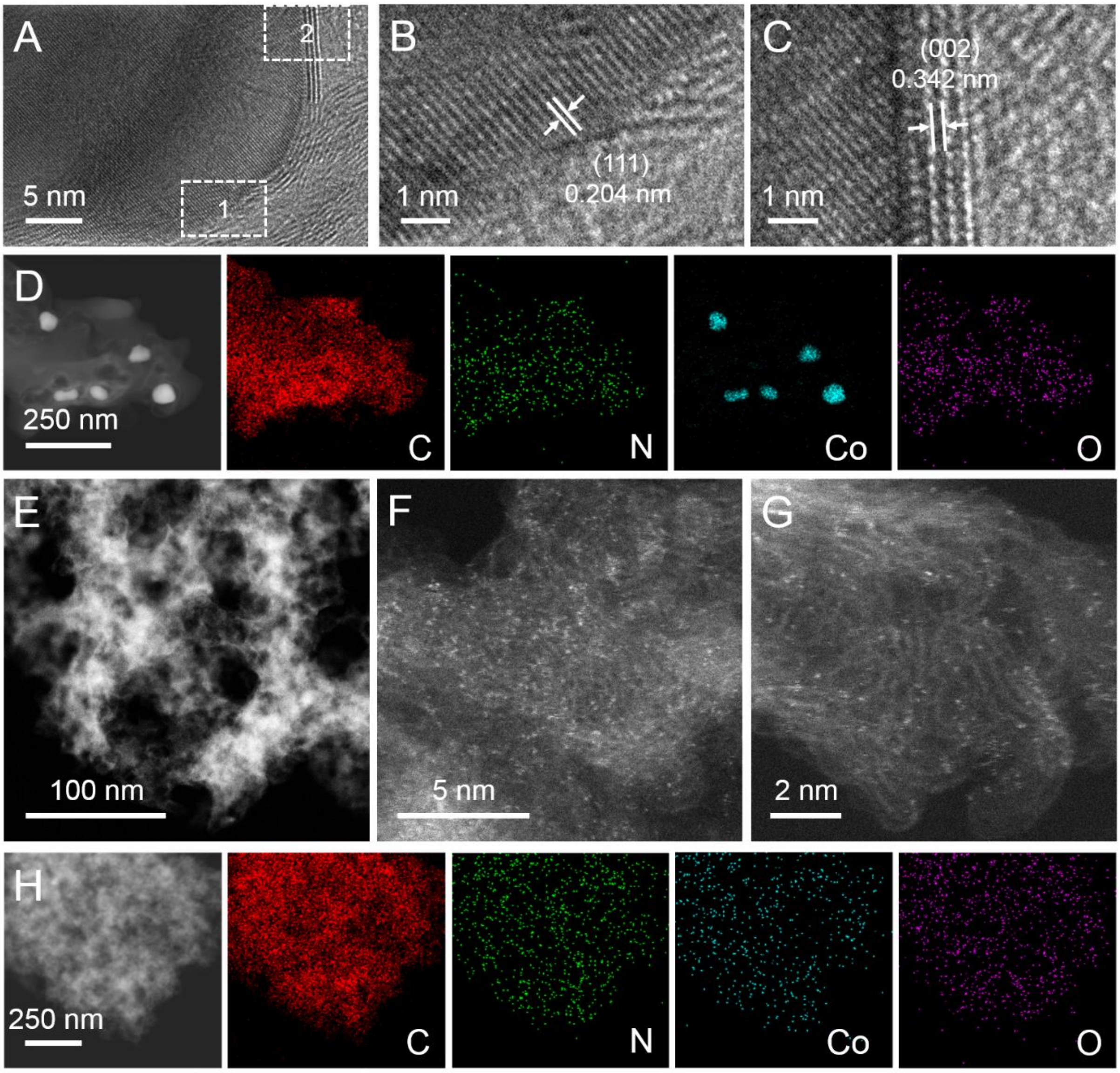

Fig. S16. Detailed characterizations of CM-DBrPhen/Co and CM-DBrPhen/Co/SiO$_2$ catalysts. (A) HRTEM image of CM-DBrPhen/Co; **(B)** Magnified HRTEM image of section 1 in **A**; **(C)** Magnified HRTEM image of section 2 in **A**; **(D)** STEM-EDS elemental mapping images of CM-DBrPhen/Co; **(E)** HAADF-STEM image of CM-DBrPhen/Co/SiO$_2$; **(F, G)** aberration-corrected HAADF-STEM images of CM-DBrPhen/Co/SiO$_2$; **(H)** STEM-EDS elemental mapping images of CM-DBrPhen/Co/SiO$_2$.

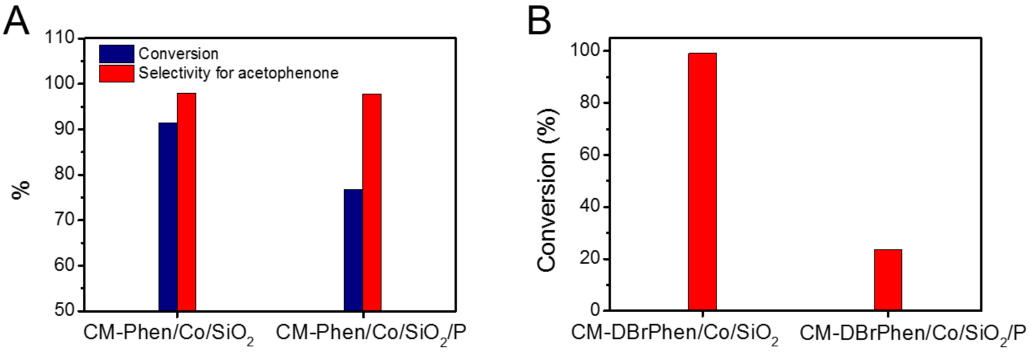

Fig. S17. The poisoning experiments for ethylbenzene oxidization and nitrobenzene hydrogenation. The poisoning experiments: **(A)** catalytic ethylbenzene oxidization performance of SCN^--poisoned CM-Phen/Co/SiO_2 (CM-Phen/Co/SiO_2/P) and CM-Phen/Co/SiO_2 catalysts; **(B)** catalytic nitrobenzene hydrogenation performance of SCN^--poisoned CM-DBrPhen/Co/SiO_2 (CM-DBrPhen/Co/SiO_2/P) and CM-DBrPhen/Co/SiO_2 catalysts.

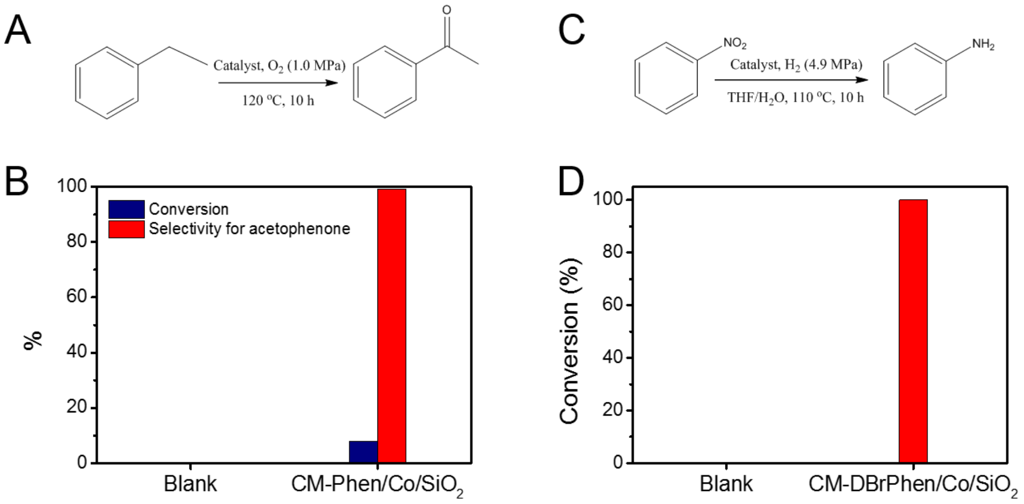

Fig. S18. Catalytic performance for selective oxidization of ethylbenzene using O_2 as the oxidant and hydrogenation of nitrobenzene using H_2 as the reductant. (A) Reaction equation of selective oxidization of ethylbenzene using O_2 as the oxidant. **(B)** Catalysis performance of CM-Phen/Co/SiO_2 for ethylbenzene oxidization. **(C)** Reaction equation of hydrogenation of nitrobenzene using H_2 as the reductant. **(D)** Catalysis performance of CM-DBrPhen/Co/SiO_2 for nitrobenzene hydrogenation.

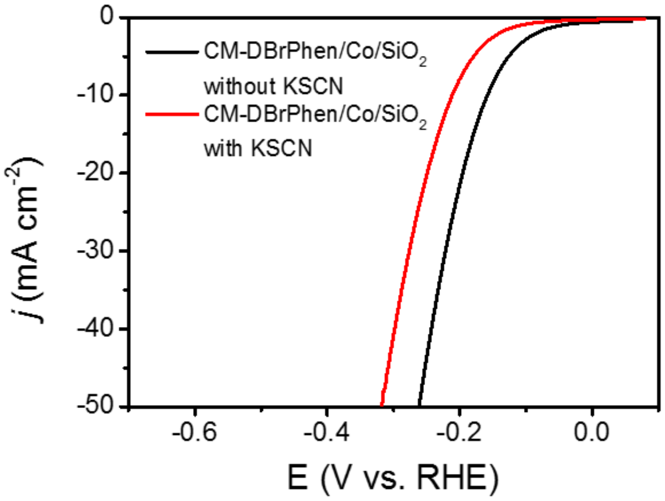

Fig. S19. The poisoning experiments for HER. The poisoning experiments: catalytic HER performance of CM-DBrPhen/Co/SiO_2 with and without 10 mM KSCN in 0.5 M H_2SO_4, indicating that SCN^- ions strongly poison the CM-DBrPhen/Co/SiO_2 catalyst.

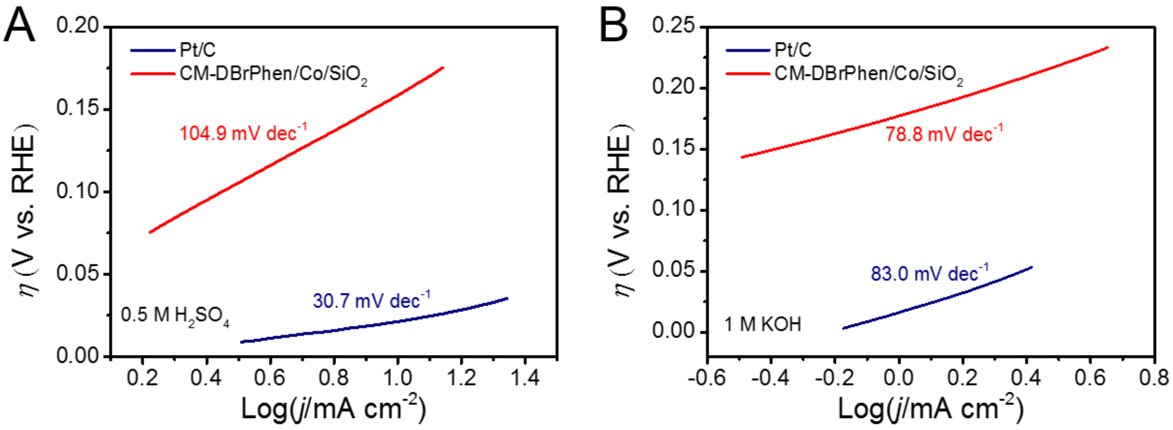

Fig. S20. Tafel curves of CM-DBrPhen/Co/SiO_2 and commercial Pt/C catalyst. (A and **B)** Tafel curves of CM-DBrPhen/Co/SiO_2 and commercial Pt/C catalyst in **(A)** 0.5 M H_2SO_4 solution and **(B)** 1 M KOH solution.

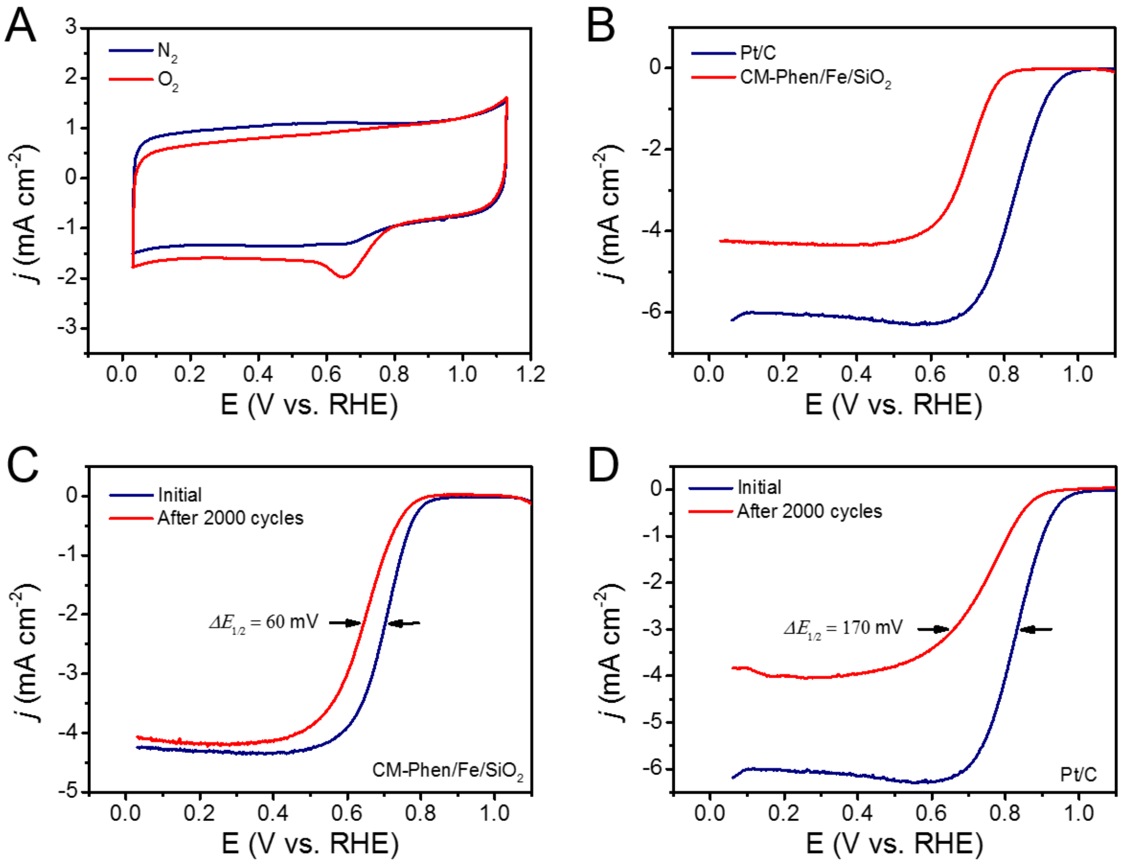

Fig. S21. Electrocatalytic performance of CMs for ORR in acidic medium. (A) CV curves of CM-Phen/Fe/SiO_2 in 0.5 M H_2SO_4. **(B)** LSV curves of CM-Phen/Fe/SiO_2 and commercial Pt/C catalyst in 0.5 M H_2SO_4. **(C, D)** LSV curves of **(C)** CM-Phen/Fe/SiO_2 and **(D)** Pt/C before and after 2000 potential cycles in O_2-saturated 0.5 M H_2SO_4.

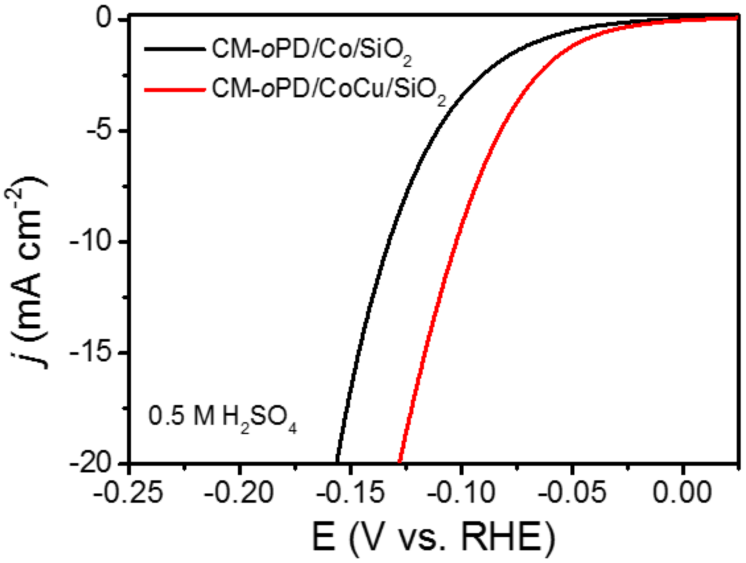

Fig. S22. HER polarization curves of CM-*o*PD/Co/SiO_2 and CM-*o*PD/CoCu/SiO_2 in 0.5 M H_2SO_4. This data clearly indicates the superior HER performance of the bimetallic CM-*o*PD/CoCu/SiO_2 catalyst.

Table S1. Summary of carbon yield, texture properties, elemental composition of CMs prepared with $Co(NO_3)_2$ as the catalyst.

SOM	TGA carbon yield (%)	TGA relative carbon yield (%)	Oven carbon yield (%)	Oven relative carbon yield (%)	S_{BET} (m^2 g^{-1})	Pore volume (cm^3 g^{-1})	Surface composition (wt%)	Co content (wt%)
DCD	5.61	19.63	5.88	20.58	138	0.46	C-87.17 N-4.20 O-6.37 Co-2.26	11.09
4-MI	11.78	20.15	15.70	26.83	138	0.34	C-87.36 N-3.03 O-7.26 Co-2.35	9.85
Mel	5.77	20.19	5.65	19.76	65	0.30	C-87.94 N-3.81 O-6.18 Co-2.08	2.69
*o*PD	65.63	98.44	55.63	83.44	325	0.28	C-92.60 N-1.69 O-5.32 Co-0.39	3.73
BP	33.91	50.86	29.01	43.51	209	0.14	C-93.84 N-0.67 O-3.90 Co-1.58	23.36
*o*DHB	27.22	41.59	23.94	36.58	192	0.24	C-93.63 N-0.31 O-5.34 Co-0.72	11.79
BPy	7.81	10.15	4.20	5.46	/	/	C-90.84 N-1.31 O-4.96 Co-2.88	11.30
DBrBPy	35.71	93.37	32.53	85.04	696	0.07	C-80.92 N-5.70 O-12.02 Co-1.35	2.06
BPym	15.65	25.76	26.17	43.07	436	0.13	C-83.49 N-5.71 O-8.79 Co-2.01	9.32
BTh	/	/	25.70	47.92	201	0.08	C-55.43 N-2.13 O-15.75 S-13.35 Co-13.29	2.24
DBrBTh	/	/	23.95	80.79	248	0.03	C-66.38 N-3.33 O-12.04 S-11.73 Co-6.49	8.57
Phen	56.70	70.89	53.64	67.06	313	0.24	C-85.93 N-4.08 O-7.93 Co-2.07	7.36
DBrPhen	31.79	74.54	26.66	62.52	293	0.08	C-86.14 N-3.94 O-7.95 Co-1.98	5.40
Pah	4.60	4.88	11.70	12.40	191	0.26	C-83.52 N-1.74 O-8.38 Co-6.36	10.22
BBPy	70.03	95.56	67.20	91.70	318	0.24	C-89.93 N-2.95 O-5.69 Co-1.43	5.12

Note: carbon yield refers to the weight ratio between resultant CM and SOM; theoretical yield refers to the weight ratio between overall carbon content in the SOM and SOM; relative carbon yield refers to the ratio between carbon yield and theoretical yield.

Table S2. Carbon yields of *o*PD with different TMSs as catalysts.

TMS	TGA carbon yield (%)	TGA relative carbon yield (%)	Oven carbon yield (%)	Oven relative carbon yields (%)	mental content (%)
$Co(NO_3)_2$	65.63	98.44	55.63	83.44	3.73
$Fe(NO_3)_3$	53.25	79.87	51.98	77.96	1.74
$Cr(NO_3)_3$	49.14	73.71	44.05	66.07	14.35
H_2PtCl_6	34.64	51.96	41.30	61.94	14.32
$Cu(NO_3)_2$	32.85	49.27	35.61	53.42	15.59
$Mn(NO_3)_2$	30.27	45.41	32.46	48.68	2.81
$AgNO_3$	21.58	32.36	18.49	27.44	2.44
$Ni(NO_3)_2$	15.91	23.87	14.64	21.95	3.66
$Zn(NO_3)_2$	14.01	21.00	11.62	17.43	4.77
$SnCl_2$	0	0	0	0	/
$NaNO_3$	0	0	0	0	/
$Ca(NO_3)_2$	0	0	0	0	/

Table S3. Carbon yields of *o*PD with different amounts of $Co(NO_3)_2$ as catalysts.

TMS content	TGA carbon yield (%)	TGA relative carbon yield (%)	Oven carbon yield (%)	Oven relative carbon yields (%)
10%	65.63	98.44	55.63	83.44
5%	49.07	73.60	51.98	77.96
2%	29.10	43.65	30.83	46.24
1%	11.41	17.11	12.28	18.41
0%	0	0	0	0

Table S4. Summary of carbon yield, texture properties, and elemental composition of CMs prepared with $Co(NO_3)_2$ as the catalyst and SiO_2 nanoparticles as hard templates.

SOM	Oven carbon yield (%)	Oven relative carbon yield (%)	S_{BET} (m^2 g^{-1})	Pore volume (cm^3 g^{-1})	Surface composition (%)	Co content (%)
DCD	10.53	36.86	196	0.48	C-85.13 N-3.28 O-7.56 Co-4.03	12.91
4-MI	29.18	49.87	361	0.47	C-74.30 N-5.40 O-18.56 Co-1.74	2.40
Mel	9.31	32.58	275	0.30	C-90.94 N-2.71 O-3.89 Co-2.47	3.33
*o*PD	60.08	90.11	885	1.54	C-85.84 N-3.33 O-10.64 Co-0.19	0.99
BP	45.23	67.84	867	0.92	C-80.29 N-1.37 O-18.35	0
*o*DHB	46.02	70.32	438	1.04	C-79.57 N-1.55 O-18.88	0
BPy	21.90	28.49	382	0.61	C-81.88 N-3.85 O-11.90 Co-2.37	10.37
DBrBPy	37.17	97.17	966	1.76	C-83.49 N-6.44 O-8.71 Co-1.36	2.60
BPym	28.37	46.70	607	0.73	C-82.55 N-5.55 O-10.59 Co-1.31	7.31
BTh	45.75	79.17	1202	1.42	C-77.76 N-1.32 O-14.15 S-6.14 Co-0.63	0.19
DBrBTh	26.86	90.58	959	2.16	C-73.91 N-3.19 O-13.31 S-7.83 Co-1.76	2.01
Phen	78.62	98.30	553	0.79	C-81.52 N-4.08 O-12.45 Co-1.95	3.71
DBrPhen	45.43	106.54	667	0.66	C-83.78 N-4.72 O-10.56 Co-0.94	3.36
Pah	67.13	71.16	505	1.63	C-94.2 N-0.93 O-4.86 Co-0	3.39
BBPy	71.67	97.80	448	0.43	C-91.16 N-2.35 O-5.91 Co-0.58	1.56

Table S5. HER performance comparison. Comparison of HER performance of CM-DBrPhen/Co/SiO_2 with various non-precious HER electrocatalyts reported in the literature in 0.5 M H_2SO_4 electrolyte.

	Loading density (mg cm^{-2})	$\eta@j$ = 10 mA cm^{-2} (mV vs RHE)	Ref.
CoNi@NC	0.32	224	Angew. Chem. Int. Ed. 2015, 54, 2100
CoN_x/C	2	133	Nat. Commun. 2015, 6, 7992
Co-NRCNTs	0.28	260	Angew. Chem. Int. Ed. 2014, 53, 4372
$Co_{0.6}Mo_{1.4}N_2$	0.24	200	J. Am. Chem. Soc. 2013, 135, 19186
CoS_2/RGO-CNT	1.15	142	Angew. Chem. Int. Ed. 2014, 53, 12594
$MoSe_2$/CP	-	250	Nano Lett., 2013, 13, 3426
MoC_x nano-octahedrons	0.8	142	Nat. Commun. 2015, 6, 6512
WS_2 nanoflakes	0.35	~400	Angew. Chem. Int. Ed. 2014, 53, 7860
β-$Mo_{0.06}W_{0.94}$C/CB	0.7	220	Angew. Chem. Int. Ed. 2014, 53, 5131
CoS_2 NW	1.7 ± 0.3	145	J. Am. Chem. Soc. 2014, 136, 10053
Cu_3P nanowire arrays	15.2	143	Angew. Chem. Int. Ed. 2014, 53, 9577
$CoMoS_x$	-	~210 (H_2SO_4, pH=1)	Nat. Mater. 2016, 15,197
mPF-Co-MoS_2-16.7	0.5	156	Nat. Commun. 2017, 8, 14430
Fe-WCN	0.4	220	Angew. Chem. Int. Ed. 2013, 52, 13638
$CoMoS_3$	0.5	171	Adv. Mater., 2016, 28, 92
MoS_2/$CoSe_2$	0.28	68	Nat. Commun. 2015, 6, 5982
g-C_3N_4 nanoribbon-G	0.143	207	Angew. Chem. Int. Ed. 2014, 53, 13934
MoP	0.86	140	Energy Environ. Sci., 2014, 7, 2624
Ni_2P	1.0	187	J. Am. Chem. Soc. 135, 25, 9267
CM-DBrPhen/Co/SiO_2	**0.6**	**158**	**This work**

Note S1. The proposed mechanism for different microstructures of CM-*x*/Co samples.

Although the same heating process was performed for all SOM/$Co(NO_3)_2$ precursors, the distinctly different molecular structures of SOMs make them experience different polymerization and pyrolysis processes, thus leading to different morphologies. In most cases, irregular CMs were formed, as the result of thermal polymerization of SOMs in random orientations. In the cases of 4-MI/$Co(NO_3)_2$, *o*PD/$Co(NO_3)_2$, Phen/$Co(NO_3)_2$, and Pah/$Co(NO_3)_2$, CMs with nanosheet structures were obtained. This is probably due to the formation of linear polymeric intermediates during the pyrolysis process, which tend to form sheet structure as the result of strong π-π interactions between these linear polymeric intermediates (*55*, *56*). In the cases of CM-DCD/Co and CM-Mel/Co, bamboo-like CNTs structures were obtained. It is well known that graphitic carbon nitride nanosheets were formed upon the heat-treatment of DCD or Mel at ca. 500 °C (*57*, *58*). With the increase of carbonization temperature, Co nanoparticles coated with a few carbon layers (Co@C) appeared. These Co@C-based nanoparticles produced at high temperature, demonstrated for the synthesis of CNTs by the chemical vapor deposition method (*59*, *60*), could act as catalyst for the growth of bamboo-like CNTs at an elevated temperature.

Note S2. Synthesis of high–surface area CMs from SOMs with SBA-15 as templates. Figures S5A, S5B show the TEM images of CM-*o*PD/Co/SBA-15 and CM-Phen/Co/SBA-15 prepared by using SBA-15 as the hard templates. Both of two CMs well inherit the mesostructural order of the parent SBA-15 templates, which is also confirmed by nitrogen adsorption/desorption isotherms and pore size distribution curves (figs. S5C, S5D). The well-defined capillary condensation step at 0.4-0.9 P/P_0 for CM-*o*PD/Co/SBA-15 and CM-Phen/Co/SBA-15 is indicative of a well-developed mesoporosity. Besides, the pore size distribution curves reveal that the mesopore size distribution is centered at 4.2 nm for CM-*o*PD/Co/SBA-15, and 4.5 nm for CM-Phen/Co/SBA-15, respectively. The BET surface area and total pore volume for CM-*o*PD/Co/SBA-15 and CM-Phen/Co/SBA-15 are 619 m^2 g^{-1} and 0.44 cm^3 g^{-1}, and 737 m^2 g^{-1} and 0.73 cm^3 g^{-1}. These results clearly demonstrate that SBA-15 as another hard template is also applicable to prepare porous CMs with high surface area.

Note S3. Detailed characterization analysis of CM-Phen/Co, CM-Phen/Co/SiO_2, CM-DBrPhen/Co, and CM-DBrPhen/Co/SiO_2.

The XRD patterns confirm the presence of the graphitic carbon and a Co phase in CM-Phen/Co and CM-DBrPhen/Co (fig. S14). The strong peak at ca. 26.3^o was assigned to the (002) plane of graphitic carbon, while the other diffraction peaks including 44.3^o, 51.7^o and 76.0^o agree well with those of crystalline Co (JCPDS 15-0806). However, only one peak of graphitic carbon at ca. 26.3^o is observed for CM-Phen/Co/SiO_2 and CM-DBrPhen/Co/SiO_2. The absence of crystalline Co in CM-Phen/Co/SiO_2 and CM-DBrPhen/Co/SiO_2 indicates that the Co species exist in the form of ultrasmall nanoclusters or single atoms. The SiO_2 templates facilitate the dispersion of metal species during the carbonization of SOMs and thus avoid efficiently the formation of encapsulated cobalt-containing nanoparticles that survive finally in the cases of CM-Phen/Co and CM-DBrPhen/Co (*12*).

The high-resolution transmission electron microscopy (HRTEM) image of CM-Phen/Co reveals that the Co nanoparticle is embedded with the graphitic carbon shells (fig. S15A). The spacing of crystalline lattices in two directions are 0.203 nm and 0.176 nm for the embedded nanoparticle, matching well with the (111) and (200) planes of Co phase (fig. S15B). Besides, the graphite-like layers could easily identified at the shells with an interlayer spacing of 0.34 nm, corresponding to (002) plane of graphitic carbon (fig. S15C).

Furthermore, scanning transmission electron microscopy-energy dispersive spectroscopic (STEM-EDS) elemental mapping revealed the homogenous distribution of N and O over the whole carbon matrix in CM-Phen/Co, while Co mainly exist in the nanoparticle sections (fig. S15D). Clearly, the CM-DBrPhen/Co exhibits the same microstructures to that of CM-Phen/Co (figs. S16A-S16D), and they are consisted of Co nanoparticles embedded with N-doped carbons.

For CM-Phen/Co/SiO_2 and CM-DBrPhen/Co/SiO_2, HAADF-STEM images further confirm the absence of inorganic nanoparticles (fig. S15E and fig. S16E). Aberration-corrected HAADF-STEM images with sub-angstrom resolution show that the brighter spots assigned to the Co atoms dominantly present the atomic dispersion in CM-Phen/Co/SiO_2 and CM-DBrPhen/Co/SiO_2 (figs. S15F, 15G and figs. S16F, S16G). In addition, STEM-EDS elemental mapping further reveal that CM-Phen/Co/SiO_2 and CM-DBrPhen/Co/SiO_2 are a type of catalysts with exclusive single atom Co supported on N-doped carbons (fig. S15H and fig. S16H), which are believed to contribute to highly active Co-N_x active sites, as revealed previously by X-ray absorption spectroscopy (*61*, *62*).

Note S4. Electrocatalytic performance of CMs for ORR.

In N_2-saturated electrolyte, the CV curve of CM-Phen/Fe/SiO_2 displayed featureless slopes for cathodic current (fig. S21A). In contrast, the CV curve in O_2-saturated electrolyte showed a well-defined cathodic peak centered at 0.65 V, suggesting a pronounced electrocatalytic activity for ORR. As shown by the LSV curve, the CM-Phen/Fe/SiO_2 catalyst exhibited a high ORR activity with a half-wave potential of 0.70 V versus RHE in acidic medium (fig. S21B), which is comparable to that of reported highly active non-Pt ORR catalyst (*11, 38, 63–65*). Furthermore, the accelerated durability tests showed that the CM-Phen/Fe/SiO_2 catalyst had a much better stability than Pt/C catalyst (figs. S21C, S21D). After 2000 continuous potential cycles, the half-wave potential of CM-Phen/Fe/SiO_2 exhibited a negative shift of only 60 mV, much lower than that of Pt/C catalyst (170 mV negative shift). Besides, the ORR performance of our developed CMs could be further improved by careful selecting precursors and optimizing synthetic parameters.